

Cite this: *J. Mater. Chem. C*, 2023, **11**, 6034

# Ti<sub>3</sub>AlC<sub>2</sub> MAX phase conversion to a novel 2D titanium carbo-oxide by an eco-friendly and low-cost method: highly selective gas sensing and supercapacitor evaluations

Roussin Lontio Fomekong,<sup>\*ab</sup> Jalal Azadmanjiri,<sup>id b</sup> Joyce Boitumelo Matsoso,<sup>b</sup> Marco Serra,<sup>b</sup> Sana Akir,<sup>b</sup> Lukáš Dekanovsky,<sup>b</sup> Jan Luxa,<sup>b</sup> Eva Vejmelková<sup>c</sup> and Zdeněk Sofer<sup>id \*b</sup>

Energy shortage and environmental pollution issues are among the biggest challenges of this century. Therefore, research into innovative new materials to overcome such issues is urgently required. In this context, this study reports the one-pot synthesis of a novel 2D titanium carbo-oxide layered structure using a simple and eco-friendly method. Then, its potential applications as a gas sensor and supercapacitor were evaluated for the first time. The 2D titanium carbo-oxide layered structure was prepared via a solvothermal method by exfoliation of the Ti<sub>3</sub>AlC<sub>2</sub> MAX phase with tetramethylammonium hydroxide. X-ray diffraction, Raman spectroscopy, scanning electron microscopy, and X-ray photoelectron spectroscopy characterizations demonstrated that pure 2D titanium carbo-oxide flakes with a layered structure were successfully obtained. The synthesized nanomaterial showed a very good sensing response and high selectivity towards methanol at room temperature against ethanol and other volatile organic compounds. The investigation of its supercapacitor performance in three different aqueous electrolytes revealed that this 2D nanomaterial had a high potential window of 1.8 V in Na<sub>2</sub>SO<sub>4</sub>, high specific capacitance of 161 F g<sup>-1</sup> in H<sub>2</sub>SO<sub>4</sub>, and 87.1% capacitance retention after 2500 cycles in KOH. The probably reduced interlayer spacing can explain the underlying mechanism of the sensor and its electrochemical capacitance.

Received 6th February 2023,  
Accepted 29th March 2023

DOI: 10.1039/d3tc00436h

rsc.li/materials-c

## 1. Introduction

Owing to the ever-increasing global population, energy shortage and environmental pollution issues have become research hot topics attracting the attention of more scientists.<sup>1–5</sup> Also, over the past decades, there has been a tremendous development of modern electronic devices, such as smartphones, tablets, and wearable devices. The over-consumption of these products has made the design of high-performance energy storage accessories highly important.<sup>6,7</sup> One of the best-known energy storage devices that have received a lot of attention are supercapacitors. This is due to their many advantages, such as charge/discharge capabilities, high power densities, and long cycle life.<sup>8,9</sup> On the other hand, human activities, such

as industrialization, mining, urbanization, and exploration, are responsible for the increase of air pollutants, such as NO<sub>x</sub>, CO, SO<sub>2</sub>, and volatile organic compounds (VOCs).<sup>10,11</sup> Among the VOCs, methanol is one of the most poisonous gases, and needs to be strictly controlled in the environment.<sup>12</sup> If methanol is not treated immediately after inhalation or ingestion, it can provoke irreversible tissue damage, especially to the eyes and nervous system. On the other hand, there are many potential sources of methanol in everyday life, such as adulterated alcohol and chemical raw materials in laboratories and chemical plants, hence, there is a high potential risk of poisoning in such environments.<sup>13</sup>

In order to solve all these energy storage and environmental problems, there has been a lot of interest devoted to the development of performant materials. Although many efforts have already been devoted to developing high-performance materials for supercapacitors and gas sensors, there is still a constant search to improve the performance and production costs of functional materials.<sup>14–18</sup> Among the best-known conventional nanostructured materials are two-dimensional (2D) nanomaterials, which have attracted increased interest due

<sup>a</sup> Higher Teacher Training College, University of Yaounde I, P.O. BOX 47, Yaounde, Cameroon. E-mail: lonforou@yahoo.fr/roussin, lontio@univ-yaounde1.cm

<sup>b</sup> Department of Inorganic Chemistry, University of Chemistry and Technology, Technická 5, Prague, 16628, Czech Republic. E-mail: zdenek.sofer@vscht.cz

<sup>c</sup> Department of Materials Engineering and Chemistry, Faculty of Civil Engineering, Czech Technical University in Prague, Thakurova 7, 16629, Prague, Czech Republic



to their outstanding electrical, magnetic, and mechanical properties.<sup>19,20</sup> In 2011, a new family of 2D transition metal carbides, nitrides, and carbonitrides (MXene) represented by the general formula of  $M_n + 1X_nT_x$  ( $n = 1, 2, 3, \text{ or } 4$ ), where M is an early transition metal, X is carbon and/or nitrogen, and  $T_x$  is the surface terminal groups, such as  $-O$ ,  $-OH$ , and/or  $-F$  species, was discovered. This type of 2D nanomaterial has unique characteristics, such as abundant surface functional groups, high metallic conductivity, high specific surface area, good hydrophilic nature, and good thermal stability. These characteristics make it a promising candidate in diverse high-technology applications, such as the electrodes of supercapacitors and as a sensing layer for gas sensors.<sup>21,22</sup> However, most common synthesis method for MXenes involve etching of the MAX phase *via* highly concentrated hydrofluoric acid, which, in addition to being highly toxic, generally leads to a high content of  $-F$  termination groups on the surface of the material, thus negatively affecting the performance of the supercapacitors.<sup>23</sup> All this limits the scaled-up large-scale, real-world applications of MXene. Some reports have shown that the post-treatment of MXene with a basic solution, such as KOH, can reduce the amount of  $-F$  and improve the performance of the supercapacitors.<sup>24</sup> Therefore, the development of totally new 2D materials or new scalable methods that can lead to a significantly low content or even fully eliminate the  $-F$  termination group are strongly needed for achieving high-efficiency devices. Besides, MXene has also demonstrated good sensing properties due to its high metallic conductivity for low noise, large surface area, and fully functionalized surface for achieving a strong signal.<sup>22,25</sup> In fact, most sensing materials, such as semiconducting metal oxides, have drawbacks, such as a high operating temperature and low selectivity, and these factors limit their practical applications.<sup>14,26</sup> Although some reports have shown the use of MXene for VOC detection at room temperature, the selectivity still needs to be improved.<sup>27</sup> The problem of selectivity in VOCs detection is more difficult, especially against ethanol, because all of them are reducing gases and have the tendency to react in the same way with the sensing material.

A recent research work published by Hussein O. Badr *et al.*<sup>28</sup> reported an interesting route to produce novel 2D titanium carbo-oxide flakes using the  $Ti_3AlC_2$  MAX phase with tetramethylammonium hydroxide (TMAOH,  $C_4H_{13}NO$ ) by a simple wet chemistry method for battery and biomedical applications. As a first piece of work on these new 2D nanomaterials (with the MXene-like structure but are not MXene), further investigation is needed to understand and expand their application. Moreover, the synthesized nanomaterials in that research work also were impure and the minimum reaction time was 24 h, and these deficiencies require further development. Furthermore, depending on the reaction conditions, the obtained nanomaterials were either conductive or non-conductive, due to the differences in point defects. To the best of our knowledge, the present research work reports for the first time the one-pot preparation of a pure 2D titanium carbo-oxide layered structure using a simple solvothermal method, as well as its gas-sensing and supercapacitor properties. The projected straightforward preparation process, which involves

only one step and the utilization of a cheap and eco-friendly solvent (TMAOH), shows good prospects for the large-scale production and real-world application of this material. The prepared 2D nanomaterial demonstrated very good selective methanol vapour sensing properties at room temperature, which may be useful for environmental monitoring as well as for the non-invasive assessment of gut bacterial activity by measuring methanol in exhaled breath. The evaluation of its supercapacitor potential in three different electrolytes, namely basic (KOH), neutral ( $Na_2SO_4$ ), and acidic ( $H_2SO_4$ ), using a free-binder electrode demonstrated that KOH was the most effective solution to obtain high electrochemical performance. The observed properties were probably related to the composition, point defects, and the interlayer spacing of the 2D titanium carbo-oxide electrodes.

## 2. Experimental section

### 2.1. Preparation of 2D titanium carbo-oxide flakes

The as-received  $Ti_3AlC_2$  MAX phase material (Jinzhou Haixin Metal Materials, China) and tetramethylammonium hydroxide (TMAOH,  $C_4H_{13}NO$ ), as a 10 wt% solution in  $H_2O$  (Lachema, Czech Republic), were used without further purification. In a typical synthesis, 0.97 g of  $Ti_3AlC_2$  and 9.1 g of TMAOH ( $Ti_3AlC_2$ :TMAOH = 1:2) were mixed, stirred for 30 min, and then transferred into a 50 mL Teflon-lined stainless steel autoclave. The autoclave was kept in an electric oven at 170 °C for 12 h. After the solvothermal treatment, the autoclave was cooled down to room temperature under ambient conditions. The obtained dark black sediment was collected and rinsed with ethanol, and then shaken and centrifuged at 3500 rpm four times until a clear supernatant was obtained with a pH value of 7. Once the supernatant became clear (inset Fig. 2a), 30 mL deionized water was added to the washed products, which were shaken for 5 min, followed by centrifugation at 3500 rpm (1315 rcf) for 30 min and again at 8000 rpm (6869 rcf) for 20 min, and finally the last time at 10000 rpm (10733 rcf) for 10 min. A stable colloidal suspension was obtained (see inset Fig. 2a), while the unreacted powders eventually settled down.

### 2.2. Materials characterization

The suspension was drop-cast on a suitable substrate and an X-ray diffraction instrument (XRD, Bruker D8 Advance, Germany) equipped with a  $CuK\alpha$  ( $\lambda = 1.5406 \text{ \AA}$ ) source was used to determine the crystal structure of the synthesized material. The measurements were performed in the  $2\theta$  range of 5–90°, with a step size of 0.05°. A Raman spectrophotometer from Renishaw was used to measure the Raman spectra using a 532 nm laser, 50× magnification objective, and 0.75 mW laser power in order to avoid powder degradation and the formation of any  $TiO_2$  polymorph. The measurements were performed in different locations, with an exposure time of 20 s. A scanning electron microscopy system (SEM) with an FEG electron source (Tescan Maya) was used to investigate the morphology of the material. An EFTEM Jeol 2200



FS microscope (Jeol, Japan) was used for the HR-TEM measurements and the experiments were performed at an acceleration voltage of 200 keV. An SDD detector (X-MaxN 80 TS) from Oxford Instruments (UK) was used to obtain the elemental maps and EDS spectra. The suspension was drop-cast on a TEM grid (Cu; 200 mesh; Formvar/carbon) and dried in a vacuum oven at 60 °C for 120 min. The oxidation state of the elements and surface composition of the sample were determined by X-ray photoelectron spectroscopy (XPS) analysis. The experiment was performed with an electron spectroscopy for chemical analysis (ESCA) Probe P spectrometer (Omicron Nanotechnology, Germany) using a monochromatized Al K $\alpha$  X-ray source (1486.7 eV).

### 2.3. Gas-sensor preparation

The gas-sensing properties towards VOCs were investigated by electrochemical impedance spectroscopy (EIS) using a gold interdigitated electrode (IDE) ED-IDE3-Au (Microflux Fluidic, Spain). The IDE was made with bars measuring 0.5  $\mu\text{m}$  wide and with a gap of 0.5  $\mu\text{m}$  between each other. In order to prepare the sensor, the IDE was first ultrasonically cleaned by deionized water, ethanol, and acetone and then dried in a nitrogen flow. The suspension of the sensing materials was drop-cast (2 drops) onto the preheated electrodes, dried at 90 °C for 10 min, and placed in a 20 mL chamber. For the experiments, the corresponding amount of each analyte (methanol,  $\geq 99.9\%$ ; ethanol,  $\geq 98\%$ ; acetone,  $\geq 97\%$ ; isopropanol,  $\geq 98\%$ ; *n*-butanol,  $\geq 99\%$ ; and toluene,  $\geq 98\%$ , all from Lachner) was introduced in the 20 mL chamber and 5 min was left for vapor saturation before each measurement (Fig. 1a). The responses based on the EIS measurements were acquired in the 1–106 Hz frequency range using the Metrohm Autolab potentiostat controlled by Nova 2.14 software. After measurement, 5 min was also left for the recovery. The gas concentration of the analyte was calculated using eqn (1)

$$C_{\text{ppm}} = (2.46 \times V_a \times \rho \times 10^7) / (V_c \times M_w) \quad (1)$$

where  $V_a$  represents the volume (in  $\mu\text{L}$ ) of the analyte added to the chamber,  $V_c$  is the volume (in mL, 20 mL) of the analysis chamber,  $\rho$  is the density of the analyte (in  $\text{g mL}^{-1}$ ), and  $M_w$  is the molecular weight of the analyte in  $\text{g M}^{-1}$ . From an average of two fabricated electrodes, the sensor response ( $R_{\text{esp}}$ ), was determined using eqn (2).

$$R_{\text{esp}} = (Z_0 - Z_f) \times 100 / Z_0 \quad (2)$$

### 2.4. Supercapacitor preparation

Before the measurements, the synthesized titanium carbide was initially spray-coated on to flexible large clean carbon cloth (Kynol Europa GmbH) in order to obtain a uniform thin film. Since the material would form a stable suspension in water, no additives were added before its insertion in the spray gun followed by the spraying *via* a straightforward and easy process. After the spray process, the coated carbon clothes were dried for 48 hours in a vacuum oven at 35 °C followed by punching in a small circle shape with a diameter of 10 mm as the supercapacitor electrodes. A full cell was made by assembling two electrodes (small circles shape) separated by a Whatman cellulose membrane filter previously immersed in the electrolyte (Fig. 1b).

An Autolab PGSTAT 204 system (Utrecht, Netherlands, NOVA Version 2.1.4) was used to investigate the supercapacitor properties in a two-electrode based system using three different electrolytes (1 M H<sub>2</sub>SO<sub>4</sub>, 1 M KOH, and 1 M Na<sub>2</sub>SO<sub>4</sub>). The electrochemical measurements were performed at room temperature and the electrochemical performances were evaluated using cyclic voltammetry (CV), galvanostatic charge–discharge (GCD), and electrochemical impedance spectroscopy (EIS). For each electrolyte, GCD was recorded between the corresponding potential window at different current densities (0.16–2.45 A g<sup>-1</sup>) and CVs at different scan rates (10–100 mV s<sup>-1</sup>). EIS measurements were recorded between 10 mHz and 100 kHz by an open-circuit potential at 10 mV. Based on the GCD curves, the specific capacitances ( $C_s$  in F g<sup>-1</sup>) of the electrodes were calculated using eqn (3) below:

$$C_s = (I \times \Delta t) / (m \times \Delta V) \quad (3)$$

where  $I$ ,  $m$ ,  $\Delta V$ , and  $\Delta t$  are the applied current (A), mass of the electrode materials (g, without the carbon cloth substrate collector), actual potential window (V), and discharge time (s), respectively. Moreover, the energies and power densities ( $E$  and  $P$ ) of the supercapacitor cells were calculated using the following eqn (4) and (5):

$$E_{\text{cell}} = (C_{\text{cell}} \times \Delta V^2 \times 1000) / (2 \times 3600) \quad (4)$$

$$P_{\text{cell}} = (E_{\text{cell}} \times 3600) / \Delta t \quad (5)$$

where  $E_{\text{cell}}$ ,  $C_{\text{cell}}$ ,  $\Delta V$ ,  $P_{\text{cell}}$ , and  $\Delta t$  are the energy density, specific capacitance, voltage window, power density, and discharge time. In order to compare the cycling stability of the supercapacitor in the three electrolytes, 2500 cycles were performed at a scan rate of 0.49 A g<sup>-1</sup>.

## 3. Results and discussion

### 3.1. Materials characterization

Fig. 2a shows the phase compositions of the as-received MAX phase and the synthesized nanomaterials. The main observed diffraction peaks for the MAX phase appeared at 9.5°, 19°, 34.0°, 38.5°, 41.5°, and 70°, corresponding to the (002), (004), (101), (104), (105), and (1012) planes, respectively. These peaks could determine the pure phase for Ti<sub>3</sub>AlC<sub>2</sub> (JCPDS card no. 52-0875).

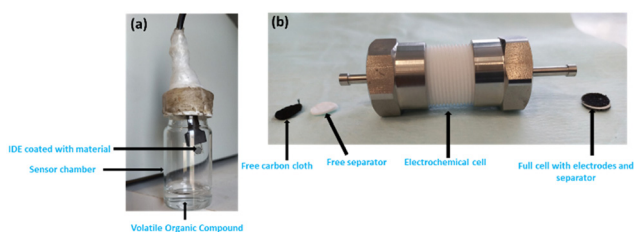


Fig. 1 Set-up for measurement of the (a) sensor and (b) supercapacitor performances.



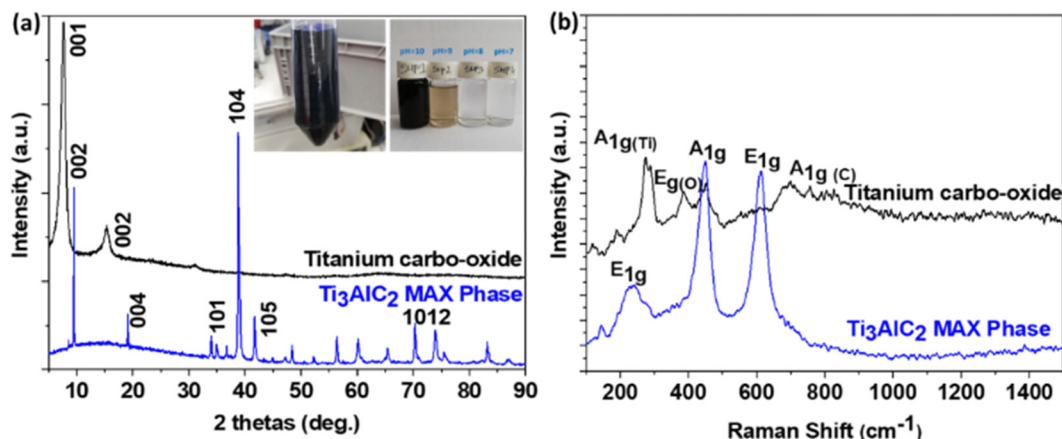


Fig. 2 (a) XRD patterns (inset shows the colloidal suspension and the different supernatants) and (b) Raman spectra of the as-received  $\text{Ti}_3\text{AlC}_2$  MAX phase and synthesized 2D titanium carbo-oxide.

After reaction with tetramethylammonium hydroxide (TMAOH,  $\text{C}_4\text{H}_{13}\text{NO}$ ), a disappearance of all the peaks was observed and two new ones emerged at  $7.5^\circ$  and  $15.3^\circ$  corresponding to (001) and (002) diffraction planes, typical of 2D materials as reported by Yibin Jiang *et al.*<sup>29</sup> This diffractogram was similar to the one reported by Hussein O. Badr *et al.*,<sup>28</sup> who synthesized the same product using a wet chemistry method under reflux conditions. However, they noticed in their diffractogram the existence of  $\text{Ti}_3\text{AlC}_2$  residue (small peaks at  $9.5^\circ$  and  $38.5^\circ$ ), which was not visible in the case of our sample. This situation confirmed the purity of the obtained product with the solvothermal method.

The Raman spectra of the  $\text{Ti}_3\text{AlC}_2$  MAX phase and the as-prepared nanomaterials are presented in Fig. 2b. It could be observed that, new vibration bands emerged in the Raman spectrum of the as-prepared nanomaterials at 276, 388, 452, and  $706\text{ cm}^{-1}$ , indicating effectively the formation of new phases. The bands observed at  $276\text{ cm}^{-1}$  ( $A_{1g}$ ) could be assigned to the

vibration of Ti atoms, the one at  $388\text{ cm}^{-1}$  ( $E_g$ ) the vibration of O atoms, and the last one at  $706\text{ cm}^{-1}$  ( $A_{1g}$ ), the vibration of C atoms. The band at  $452\text{ cm}^{-1}$  could be related to some longitudinal Ti-O vibrational modes.

The SEM and TEM images at different magnifications (Fig. 3a-d) showed the morphology of the as-prepared sample. The images show the formation of large-area flakes and a multilayered structure. The EDX mapping from the TEM image (Fig. 3c) presented in Fig. 3f revealed the presence of titanium, carbon, and oxygen as the main elements, which were homogeneously distributed. No aluminium was detected, proving that during the reaction between  $\text{Ti}_3\text{AlC}_2$  and TMAOH, aluminium had been totally removed, leading probably to the layered structure. Whereas in the conventional etching process, aluminium is usually removed using the very aggressive and dangerous chemical hydrofluoric acid, which makes the process non-environmentally friendly. This result confirmed the formation

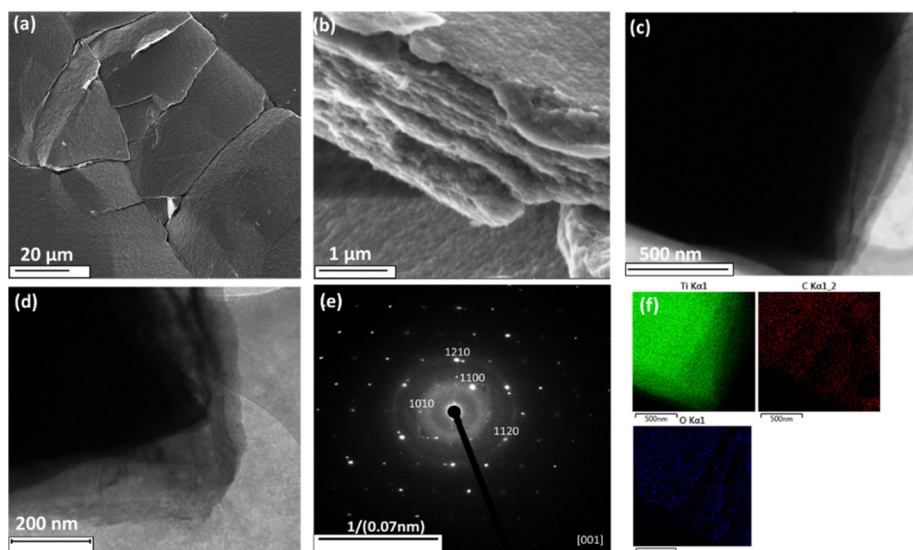


Fig. 3 Morphological characterization of the 2D titanium carbo-oxide by SEM (a and b), TEM (c and d), electron diffraction (e), and elemental mappings from TEM (f). The scale bar of the elemental mappings was 500 nm.



of a 2D titanium carbo-oxide layered structure by the applied synthetic route. Selected area electron diffraction (SAED) of the as-prepared material resulted in one main ring. After indexing, a good agreement with the XRD peaks was found, confirming the SAED patterns were representative. However, TCO still maintained a hexagonal symmetry like the parent  $\text{Ti}_3\text{AlC}_2$  sample, which was consistent with the electron diffraction pattern.

The material was further characterized by X-ray photoelectron spectroscopy (XPS), as displayed in Fig. 4. The survey spectrum in Fig. 4a revealed the presence of all the constituent elements (Ti, C, O) with no sign of Al, demonstrating its successful removal from the surface of the synthesized material. For comparison, the survey spectrum of the  $\text{Ti}_3\text{AlC}_2$  MAX phase is also shown in Fig. 4b, clearly demonstrating the presence of Al in the starting material. On the other hand, we detected a small amount of nitrogen (*ca.* 5 at%), which certainly came from the ammonium salt used during the synthesis. The high-resolution core-level spectrum of the  $\text{Ti}_{2p}$  region in Fig. 4c indicated only a single state of titanium. Based on previous reports on MAX phase  $\text{Ti}_3\text{AlC}_2$  and the respective MXene, we could conclude that this state, located at 456.8 and 462.5 eV, originated from the oxygen-terminated titanium surface (Ti-C-Ti<sub>o</sub>).<sup>17</sup> Furthermore, the presence of a single oxidation state was in high contrast to previous reports, where  $\text{TiO}_2$  was very often reported in both MAX phases as well as the respective MXenes.<sup>17</sup> The C 1s spectrum in Fig. 4d revealed two major components, one of which belonged to Ti-C bonds (282.8 eV),<sup>17</sup> while the other one (284.8 eV) was associated with adventitious carbon or carbon coming from residual salt used during the synthesis. The last component was associated with C-O bonds

coming from adventitious organic compounds. Finally, the  $\text{O}_{1s}$  spectrum in Fig. 4e also confirmed the presence of Ti-O bonds (529.6 eV) and O-C derived from adventitious organic compounds (531.6 eV).

### 3.2. Gas-sensor applications

In order to investigate the sensing properties of the as-prepared materials, first, a screening was done for the detection of many VOCs (methanol, ethanol, acetone, isopropanol, *n*-butanol, and toluene) at room temperature and the results are presented in Fig. 5. As can be observed in Fig. 5a, in air (without gases), the impedance decreased slowly from 180 to 146 Ohm with the increase in the frequency. In the presence of gas vapours, we noticed a decrease in the impedance from 180 to 42 Ohm (for methanol), 119 Ohm (for acetone), 133 Ohm (for ethanol), which were certainly due to the charge transfer between the analytes and electrode. However, compared to the blank, a lower decrease in the impedance was observed in the presence of other VOCs. In fact, since the material behaved as an n-type semiconductor, in the presence of isopropanol, *n*-butanol, and toluene, in addition to oxygen, these gases were adsorbed and were ionized by taking additional electrons on the material surface, leading to a lower decrease in the impedance compared to the blank, where only oxygen molecules were present.

Using eqn (2), the sensor responses were calculated and are presented in Fig. 5b. The response to 1500 ppm methanol (71.2%) was 3.8 times higher than that for a similar concentration of acetone (18.5%) and 8.5 times higher than that of ethanol (8.2%), confirming the very good selectivity of this sensing material towards methanol. This good selectivity could be ascribed to the small interlayer spacing of the 2D titanium

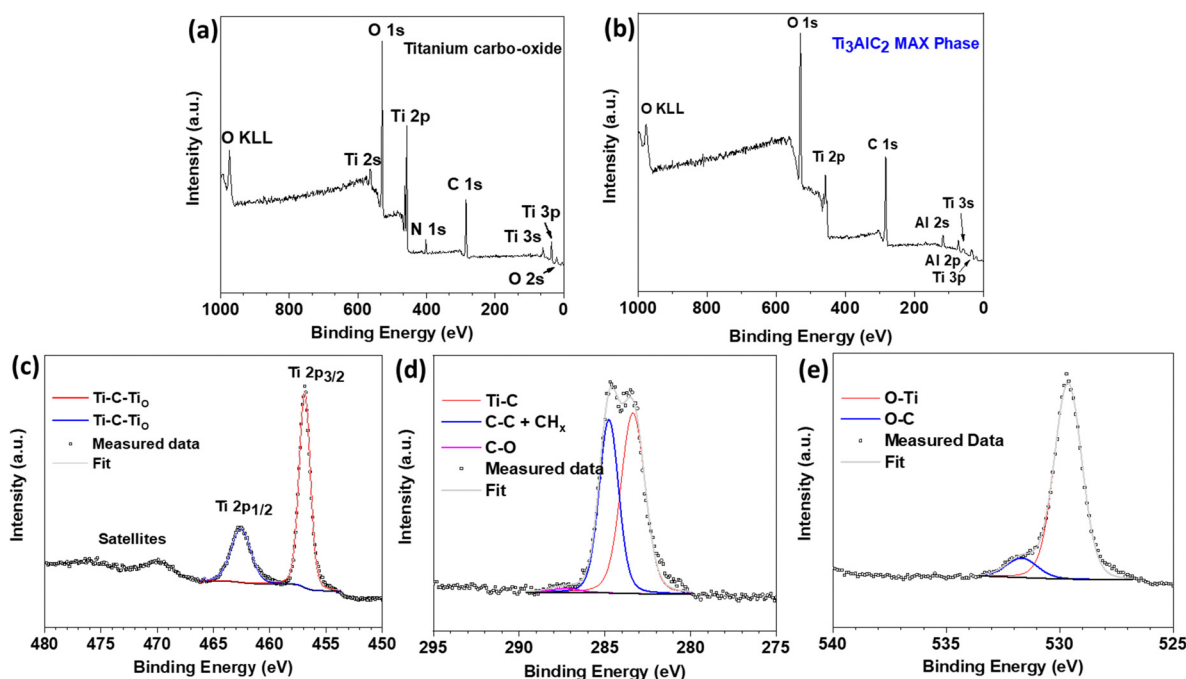


Fig. 4 XPS (a) survey spectra of the as-prepared 2D titanium carbo-oxide, (b) survey spectra of  $\text{Ti}_3\text{AlC}_2$  MAX phase, high-resolution spectra (c)  $\text{Ti}_{2p}$ , (d) C1s, and (e)  $\text{O}_{1s}$  of the as-prepared 2D titanium carbo-oxide.



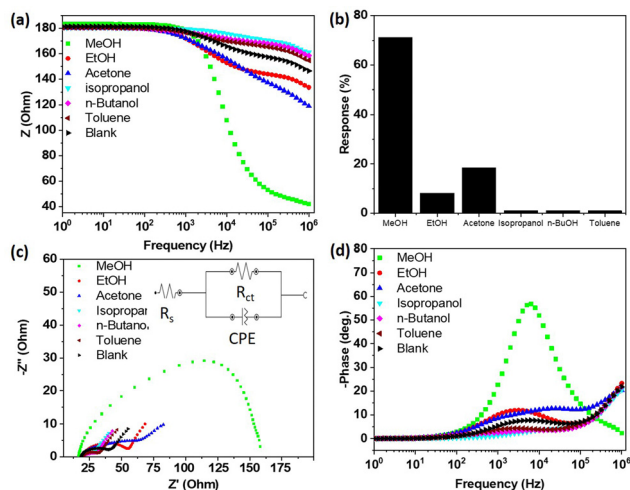


Fig. 5 (a) Variation of the impedance with the frequency. (b) Sensor responses for different VOCs. (c) Nyquist plots and (d) Bode phase plots after exposing at room temperature the as-prepared material to different VOCs at around the same concentration.

carbo-oxide prepared here, where only small molecules, like methanol (3.6 Å), could preferentially diffuse, therefore enhancing the charge transfer between methanol and the sensing layer. Due to the large sizes of the other VOCs (4.4 Å for ethanol, 6.16 Å for acetone), their diffusion in the interlayer spacing was very difficult, therefore drastically decreasing their response. Nyquist plots were recorded after exposure of all the gases to the sensing materials and the results are presented in Fig. 5c. For methanol, a single semi-cycle was obtained, indicating that the electrical interaction between the electrode and methanol followed a parallel circuit connection with the impedance resistance parallel with the double-layer capacitance. The equivalent circuit (see the inset of Fig. 5c) revealed the solution resistance ( $R_s$ ) of 44.5 Ohm, which indicated the transport properties of the accumulated methanol vapour solution-like electrolyte around the layer. The charge-transfer resistance ( $R_{ct}$ ) obtained was 140 Ohm and was related to the kinetics for the conversion of methanol to carbon dioxide and water. Since the as-prepared 2D titanium carbo-oxide was not highly conductive, a relatively high value of  $R_{ct}$  was obtained. Bode phase plots of the sensing materials were obtained (Fig. 5d) and indicated a raised affinity in sensitivity towards methanol only, whereas this trend was almost unchanged for the other vapours, confirming the good selectivity observed for methanol. This high affinity was due to the possibility for methanol to be adsorbed and to diffuse easily in the interlayer spacing, which was not the case for the bigger molecules.

To further investigate the sensor performance of the prepared materials towards methanol, the sensor responses at different concentrations of methanol were recorded and the results are depicted on Fig. 6. As can be observed, the impedance decreased less with decreasing the methanol concentration (Fig. 6a), indicating a lower charge transfer. This was also confirmed in the Nyquist plots (Fig. 6b), where  $-Z''$  decreased with decreasing the methanol concentration. The Bode phase

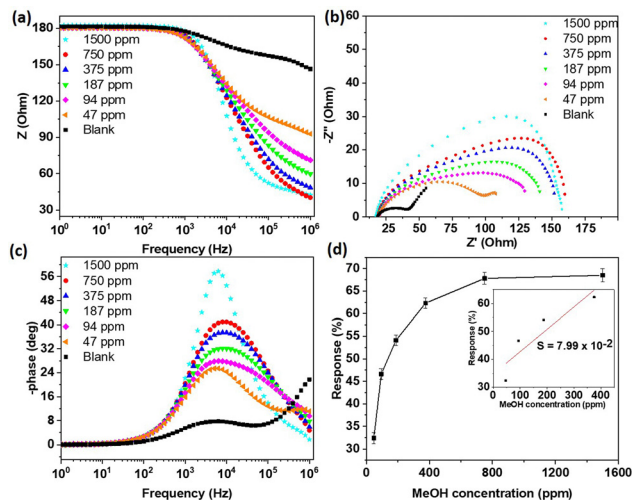


Fig. 6 (a) Variation of the impedance with the frequency. (b) Nyquist plots. (c) Bode phase plots and (d) sensor responses after exposing at room temperature the as-prepared material to different methanol concentrations.

plots (Fig. 6c) also showed a decreasing affinity of the sensing materials with methanol when its concentration decreased. As clearly depicted in Fig. 6d, the sensor response increased with the increasing methanol concentration up to 750 ppm of methanol, before becoming constant. This could be due to the saturation of the sensing layer after 750 ppm, leading to a constant charge transfer. At low concentration, it could be presumed that more methanol molecules became adsorbed on the material surface (when the methanol concentration increased), leading to an increase in the charge transfer and therefore the sensor response. As shown in Table 1, the sensing performance for the detection of methanol of the new 2D titanium carbo-oxide sensing layer reported in this study was found to be relatively comparable and even somehow better than those of the 2D materials and metal oxides. Although the impedimetric investigation on the detection of methanol is a relatively new topic, the results obtained in this work showed that 2D titanium carbo-oxide does have potential to selectively detect methanol at room temperature. It should be noted that, the cross-sensitivity was evaluated by calculating the ratio between the sensors responses obtained in the methanol with the one obtained in ethanol or acetone, which are the most interfering gases. The sensor developed in this study was 8.5 times more sensitive to methanol than ethanol, which shows it had outstanding performance. Other sensing parameters for the 2D titanium carbo-oxide were evaluated through calculation of the sensitivity ( $S = dR_{esp}/dC$ ) and concentration limit of detection ( $LoD = 3.3 \times \sigma/S$ ,  $\sigma$  is the standard deviation) as per the plots of the sensor response ( $R_{esp} = (Z_0 - Z_t) \times 100/Z_0$ ) against the concentration of the analyte (Fig. 6d). Using the linear part of that figure (inset Fig. 6d) a sensitivity of  $7.99 \times 10^{-2} \text{ ppm}^{-1}$  and an LoD of 2.26 ppm were obtained. The limit of our sensing system did not allow us to test experimentally this very low LoD. These values of the sensitivity and LoD are good and even better than some 2D materials operating at room temperature reported in the literature.<sup>36</sup> The stability is also an important sensing parameter



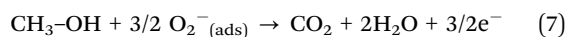
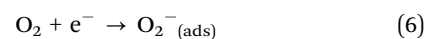
**Table 1** Comparison of the methanol sensing performance of 2D titanium carbo-oxide prepared in this work with other materials reported in the literature

Materials	Operating temperature (°C)	Selectivity against ethanol ( $R_{\text{resp-methanol}}/R_{\text{resp-ethanol}}$ )	Selectivity against acetone ( $R_{\text{resp-methanol}}/R_{\text{resp-acetone}}$ )	Ref.
L-SnS@rGO	RT	2.4	3.3	30
CNPs/ZnO@ZIF-8	RT	2.1	4.9	31
MoS <sub>2</sub> /TiO <sub>2</sub>	240	2.1	2.9	32
2D-HfS <sub>2</sub>	RT	2.2	1.8	33
Indium tungsten oxide	312	2.0	1.7	34
Mg-doped InSnO	RT	1.9	2.8	35
Titanium carbo-oxide	RT	8.5	3.8	This work

for practical application of a sensor device. The stability of 2D titanium carbo-oxide material was thus investigated by measuring the response towards methanol using our device that has been stored at room temperature. During a period of 15 days, the sensor response towards 750 ppm of methanol was measured every 2 days. As depicted in Fig. 11f, the sensor response towards 750 ppm of methanol was measured every 2 days. As depicted in Fig. 11f, the sensor response decreased slowly from 67.1% on day 1 to 58.9 on day 15, corresponding to a 12% drop in performance. This finding, which is comparable to some reported in the literature,<sup>37</sup> demonstrated that the 2D titanium carbo-oxide showed acceptable stability for the detection of methanol at room temperature.

**Sensing mechanism.** Based on the obtained results, the as-prepared 2D titanium carbo-oxide exhibited an n-type behaviour and its detection principle should follow the same trends.<sup>14</sup> Following the surface-adsorbed oxygen ions mechanism (Fig. 7a), we propose that when the sensing materials were exposed to air, the oxygen molecules were adsorbed and ionized ( $\text{O}_2^-$ ) on the surface (eqn (6)) by removing electrons, and this created an electron-depleted space charge layer. Upon exposure to reducing gases, such as methanol, followed by its adsorption and diffusion in the material, an oxidation reaction (eqn (7)) takes place and the released electrons return to the sensing layer, provoking a decrease in the thickness of the electron-depleted layer, and leading to a decrease in the impedance of the materials. The presence of defects on the titanium carbo-oxide layered structure (created during the removal of aluminium in the MAX phase) could have led to the generation of an abundance of oxygen vacancies, serving as additional adsorption sites of methanol on the surface, and leading to the increase in the sensitivity. The expected presence of -OH termination groups (an issue from the tetramethyl ammonium hydroxide during the synthesis) also favoured the adsorption of

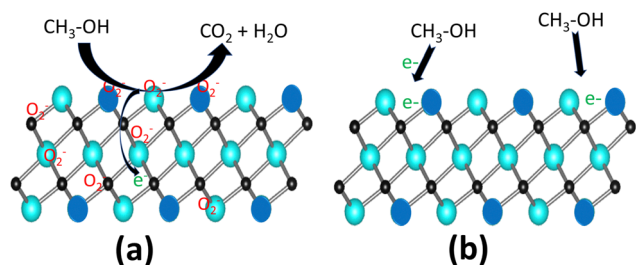
methanol due to the van der Waals interaction. The increase in the sensitivity and selectivity towards methanol could also be due to the high adsorption and diffusion of this lower molecular size of analyte in the materials due to the suitable interlayer spacing. In fact, as the sensing material had a 2D layered structure with probably small interlayer spacing, methanol could diffuse more easily in the interlayer spacing compared to the other VOCs, which are bigger. This increase in the amount of adsorbed methanol led to an increase in the released electrons after the oxidation reaction, and therefore the sensing response increased. The detection principle can also follow the charge-transfer mechanism (Fig. 7b). For this specific case, 2D titanium carbo-oxide will behave as an acceptor of charge during the detection. In fact, in the presence of methanol, the electron charges are transferred from methanol to material surface, and this will increase the electron concentration on the 2D titanium carbo-oxide, leading to the impedance decreasing.



### 3.3. Supercapacitor application

In order to fully screen the electrochemical capacitance performance of the synthesized 2D titanium carbo-oxide nano-materials in a supercapacitor device, a standard two-electrode system using 1 M KOH, 1 M H<sub>2</sub>SO<sub>4</sub>, and 1 M Na<sub>2</sub>SO<sub>4</sub> electrolytes was examined. This was because the electrolyte, which is one of the main components of supercapacitors, plays an important role in determining the safety, cost, and electrochemical performance of the overall such devices. Therefore, about 3 mg of active materials was sprayed on to each clean piece of chemically inert carbon cloth as a flexible substrate so that about 6 mg activated materials was calculated in each supercapacitor cell.

Fig. 8 shows the CV loops recorded on the cell supercapacitors in all three electrolytes at different scan rates of 10, 30, 50, 70, and 100 mV s<sup>-1</sup>. Depending on the electrolyte, the fixed potential range applied was in the ranges of 0.00–1.25 V, 0.00–0.85 V, and 0.00–1.80 V for KOH, H<sub>2</sub>SO<sub>4</sub>, and Na<sub>2</sub>SO<sub>4</sub>, respectively. We should notice that a good potential window was reached here with a neutral aqueous electrolyte, thus expanding the application range of this electrode material.

**Fig. 7** Sensing mechanism.

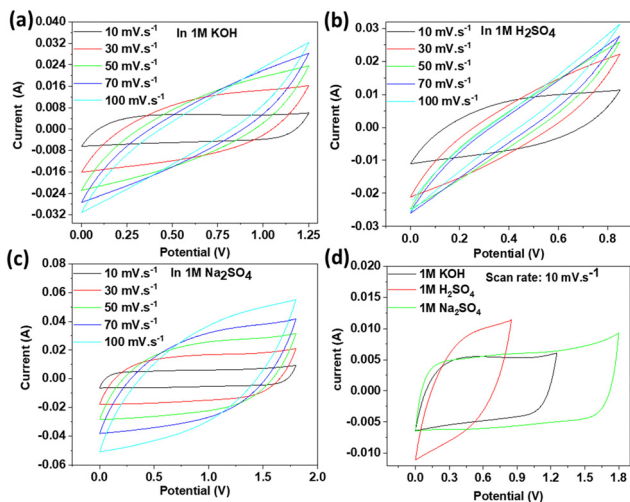


Fig. 8 CVs at various scan rates in (a) KOH, (b)  $\text{H}_2\text{SO}_4$ , (c)  $\text{Na}_2\text{SO}_4$  electrolytes and (d) comparative CV curves at a specific scan rate of  $10 \text{ mV s}^{-1}$ .

All the CV curves showed nearly rectangular-shaped loops, indicating a supercapacitor with good capacitance behaviour and with a storage mechanism based on electric double-layer capacitor (EDLC).<sup>23</sup> However, it could be observed from Fig. 8d that the rectangular loop was more distorted for  $\text{Na}_2\text{SO}_4$  and  $\text{H}_2\text{SO}_4$ , indicating that the equivalent series resistance (related to the electrode material resistance) became significant. This was certainly due to the low diffusion rate of the quite large sulfate ions within the probably reduced interlayer spacing of the active material.

Galvanostatic charge/discharge (GCD) curves were recorded for the three electrolytes and are plotted in Fig. 9. The obtained triangular GCD curves at different constant current densities ( $0.16, 0.32, 0.49, 0.82, 1.63, \text{ and } 2.45 \text{ A g}^{-1}$ ) confirmed the good capacity behaviour. However, the Coulombic efficiency obtained in KOH (93%) was higher than that of  $\text{Na}_2\text{SO}_4$  (66%)

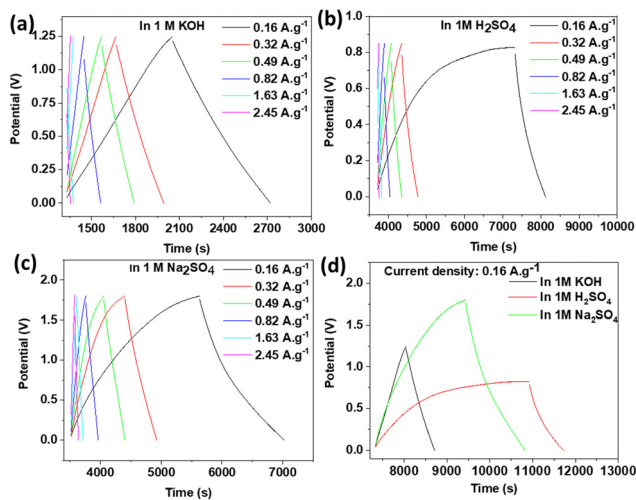


Fig. 9 GCD at various current densities in (a) KOH, (b)  $\text{H}_2\text{SO}_4$ , (c)  $\text{Na}_2\text{SO}_4$ , and (d) comparative GCD curves at a specific current density of  $0.16 \text{ A g}^{-1}$ .

and  $\text{H}_2\text{SO}_4$  (27%). The possible reason behind these differences was probably due to the small interlayer spacing for the active material, which reduced the diffusion of larger electrolyte ions like  $\text{SO}_4^{2-}$  during the intercalation/deintercalation process. The IR drop in KOH was  $0.03 \text{ V}$ , which was lower than that of  $\text{Na}_2\text{SO}_4$  ( $0.04 \text{ V}$ ) and  $\text{H}_2\text{SO}_4$  ( $0.06 \text{ V}$ ), indicating effectively the lower internal resistance when KOH was used as an electrolyte.<sup>38</sup> Fig. 9d illustrates a comparison of the GCD curves in different electrolytes, and based on this, the specific capacitances were calculated for all three electrolytes at the minimum applied current of  $0.001 \text{ A}$  using eqn (3). Taking into consideration the IR drop and the potential window for each electrolyte, the different specific capacitances were  $90 \text{ F g}^{-1}$  (for KOH),  $161 \text{ F g}^{-1}$  (for  $\text{H}_2\text{SO}_4$ ), and  $129 \text{ F g}^{-1}$  (for  $\text{Na}_2\text{SO}_4$ ). These specific capacitances were higher than for many other pristine 2D materials reported in the literature.<sup>19</sup> It already has been investigated and reported that the type of anionic and cationic species of the electrolyte affects the specific capacitance and this can explain the different values of the specific capacitances observed in this work.<sup>39</sup> Looking at the cationic species in our study, it is rational that the supercapacitor with  $\text{H}_2\text{SO}_4$  electrolyte showed the largest specific capacitance due to having the smallest hydrated  $\text{H}^+$  ion size ( $0.28 \text{ nm}$ ) and high conductivity and ionic mobility. Although  $\text{K}^+$  ( $0.331 \text{ nm}$ ) possessed a smaller hydrated ion size than  $\text{Na}^+$  ( $0.358 \text{ nm}$ ), the number of charges (two  $\text{Na}^+$  for  $\text{Na}_2\text{SO}_4$  and one  $\text{K}^+$  for KOH) explained the higher specific capacitance for  $\text{Na}_2\text{SO}_4$  in comparison to KOH. It could be observed from Fig. 9 that the Coulombic efficiency of the 2D titanium carbo-oxide supercapacitor performed better with a triangle shape in the KOH electrolyte at all the applied current densities. However, the Coulombic efficiency was not satisfactory for the initial two low current densities in the supercapacitors made by  $\text{Na}_2\text{SO}_4$  and  $\text{H}_2\text{SO}_4$  electrolytes. This undesired status of Coulombic efficiency with the last two supercapacitors may be attributed to the larger ionic size of  $\text{SO}_4^{2-}$  ( $258 \text{ pm}$ ) than  $\text{OH}^-$  ( $133 \text{ pm}$ ). The synthesized 2D titanium carbo-oxide had a high volume of surface defects, caused during the etching condition. Hence, the electrolyte ions could intercalate to the structure easily and with a greater volume at all current densities when charging the supercapacitors. The intercalated electrolyte ions, especially those with larger ionic sizes, could probably be trapped inside the 2D titanium carbo-oxide structure during the discharging and deintercalation process when a low current density is applied. Consequently, the discharge time would be lower than the charge time and this unbalance time condition would lead to poor Coulombic efficiencies at low current densities. For practical application, the energy ( $E$ ) and power ( $P$ ) densities of a supercapacitor cell should be evaluated in addition to the capacitance. Using eqn (4) and (5), the energy densities of  $18.6, 14.1, \text{ and } 55.5 \text{ W h kg}^{-1}$  and power densities of  $100.0, 62.1, \text{ and } 143.5 \text{ W kg}^{-1}$  were obtained for KOH,  $\text{H}_2\text{SO}_4$ , and  $\text{Na}_2\text{SO}_4$  respectively, at an applied current of  $0.001 \text{ A}$ . The obtained different values can be explained by the different potential windows in the three selected electrolytes, as represented in Fig. 9d ( $1.25 \text{ V}$  for KOH,  $0.85 \text{ V}$  for  $\text{H}_2\text{SO}_4$ , and  $1.8 \text{ V}$  for  $\text{Na}_2\text{SO}_4$ ).



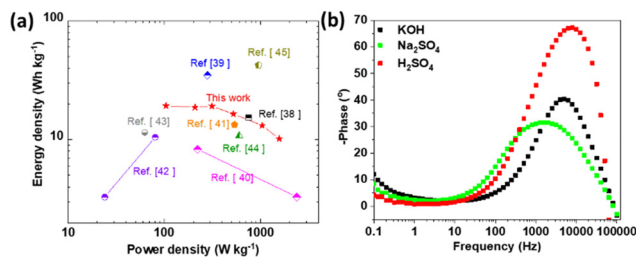


Fig. 10 (a) Ragone plots of the 2D titanium carbo-oxide supercapacitor and its comparison with the other high prestigious ref. 40–47. (b) Bode phase angle plots.

To further evaluate the overall electrochemical characteristics of the 2D titanium carbo-oxide supercapacitor, a Ragone plot (power density *versus* energy density) was plotted and is presented in Fig. 10a, which was also compared with some other references with different symmetric supercapacitor test cells. This demonstrated that the energy and power densities of the supercapacitor developed in this work were more competitive than some of the previous good reports.

The cycling stability of the three supercapacitors was also evaluated at a low current density of  $0.49 \text{ A g}^{-1}$ . As a proof of concept for this new material, we just limited the experiment to 2500 cycles. From Fig. 11b and c, it can be observed that the specific capacitance value moderately rose during the initial charge–discharge cycles, which may be associated with the precise activation of the electrode materials with the electrolytes, overcoming the internal resistances of the device. It is also evident from Fig. 11a–c that the electrode material had the best stability in KOH, with 87.1% capacitance retention value of

the initial capacitance after 2500 cycles. However, this behaviour could not be seen with the other two electrolytes where the capacitance retention was less than 31% in  $\text{Na}_2\text{SO}_4$  after 400 cycles and just 28% after 300 cycles in  $\text{H}_2\text{SO}_4$ . These differences in the cycling stabilities could be related to the anion sizes of the electrolytes and the small interlayer spacing of the 2D titanium carbo-oxide. In neutral and acidic electrolytes, the large  $\text{SO}_4^{2-}$  will have low mobility during the intercalation/deintercalation process and this will decrease the cycling stability in those electrolytes.<sup>39</sup> The other reason could be due to the large value of defects on the 2D nanomaterials, where the large ionic sizes first penetrate the material during charging the supercapacitor. However, they may be trapped inside the nanostructure materials when discharging.

Electrochemical impedance spectroscopy (EIS) was performed on the supercapacitor cells in order to understand the ion diffusion and charge transport of the active electrode materials in the three electrolytes. As shown in Fig. 11d, the Nyquist plots presented similar characteristics for the three electrolytes. However, the semicircle diameter in the high-frequency region for the KOH electrolyte was the smallest, and additionally, the oblique line of the KOH curve was closest to the vertical axis in the low-frequency region, indicating a low equivalent series resistance, which was compatible with the CV and GCD results. The inset of Fig. 11d shows the equivalent circuit for the EIS fitting curves in KOH. The value obtained for the combined resistance ( $R_s$ ), comprising the ionic resistance of the electrolyte, intrinsic resistance of electrode materials, and contact resistance between the electrode and current collector, was 2.09 Ohm, and the charge-transfer resistance ( $R_{ct}$ ) was 12.7 Ohm, which was lower than that in other electrolytes

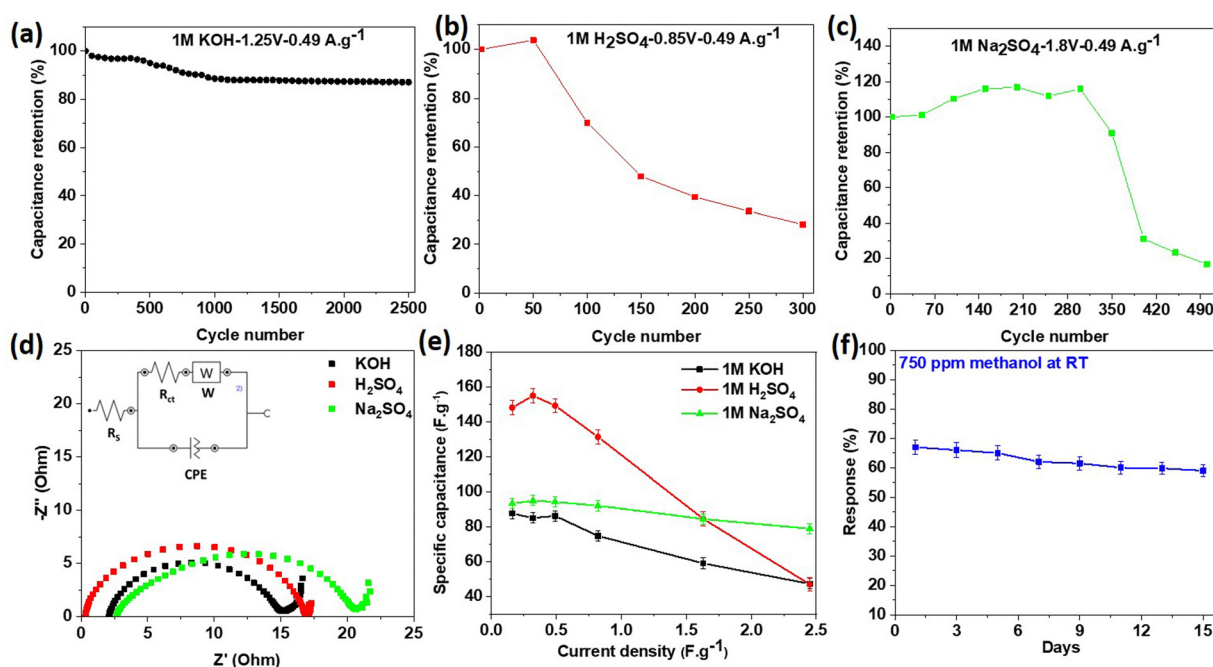


Fig. 11 Cyclic stability at a current density of  $0.49 \text{ A g}^{-1}$  in (a) KOH, (b)  $\text{H}_2\text{SO}_4$ , and (c)  $\text{Na}_2\text{SO}_4$ . (d) Comparative Nyquist plots and (e) comparative curves of specific capacitances at various current densities. (f) Stability test towards 750 ppm methanol at room temperature.



**Table 2** Comparison of the supercapacitor performances of the 2D titanium carbo-oxide prepared in this work with other materials reported in the literature

Materials	Electrolyte	Specific capacitance (F g <sup>-1</sup> )	Potential window (V)	Energy density	Power density	Ref.
Ti <sub>3</sub> C <sub>2</sub> T <sub>x</sub> /MWCNT-rGO	1 M H <sub>2</sub> SO <sub>4</sub>	48 at 2 mV s <sup>-1</sup>	1.1	8 W h kg <sup>-1</sup>	60 W kg <sup>-1</sup>	48
Microporous carbon	0.5 M Na <sub>2</sub> SO <sub>4</sub>	60 at 0.2 A g <sup>-1</sup>	1.8	7 W h kg <sup>-1</sup>	40 W kg <sup>-1</sup>	49
Mo <sub>2</sub> CT <sub>x</sub>	1 M H <sub>2</sub> SO <sub>4</sub>	79.14 at 0.3 A g <sup>-1</sup>	0.6	16.0 W h L <sup>-1</sup>	1449.1 W L <sup>-1</sup>	50
V <sub>2</sub> NT <sub>x</sub>	3.5 M KOH	112.8 at 1.85 mA cm <sup>-2</sup>	1.0	15.66 W h kg <sup>-1</sup>	3748.4 W kg <sup>-1</sup>	51
Ti <sub>3</sub> C <sub>2</sub>	6 M KOH	118 at 5 A g <sup>-1</sup>	1.4	—	—	52
carbon xerogel	1 M Na <sub>2</sub> SO <sub>4</sub>	156	1.8	17.5 W h kg <sup>-1</sup>	—	53
VS <sub>2</sub>	1 M KOH	139 at 0.7 A g <sup>-1</sup>	0.6	15.6 W h kg <sup>-1</sup>	304 W kg <sup>-1</sup>	54
Se/Ti <sub>3</sub> C <sub>2</sub> T <sub>x</sub>	1 M Na <sub>2</sub> SO <sub>4</sub>	96 at 0.17 A g <sup>-1</sup>	1.5	30 W h kg <sup>-1</sup>	124.7 W kg <sup>-1</sup>	55
Titanium carbo-oxide	1 M H <sub>2</sub> SO <sub>4</sub>	160 at 0.16 A g <sup>-1</sup>	0.9	14.1 W h kg <sup>-1</sup>	62.1 W kg <sup>-1</sup>	This work
Titanium carbo-oxide	1 M KOH	90 at 0.16 A g <sup>-1</sup>	1.3	18.6 W h kg <sup>-1</sup>	100.0 W kg <sup>-1</sup>	This work
Titanium carbo-oxide	1 M Na <sub>2</sub> SO <sub>4</sub>	129 at 0.16 A g <sup>-1</sup>	1.8	55.5 W h kg <sup>-1</sup>	143.5 W kg <sup>-1</sup>	This work

(18.4 Ohm for Na<sub>2</sub>SO<sub>4</sub> and 84.2 Ohm for H<sub>2</sub>SO<sub>4</sub>). The titanium carbo-oxide/KOH interface was equivalent to the electric double-layer capacity in the as-prepared materials supercapacitors, which expresses the constant phase element (CPE).

When increasing the current density, it was observed that the specific capacitance of the active electrode material decreased in the three electrolytes, as depicted in Fig. 11e. This general trend is in accordance with many works published in the literature.<sup>51,56</sup> In fact, when the current density increased, the charges did not have enough time to move through the interlayer spacing during the charge/discharge process, leading to the low specific capacitance. Fig. 10b presents the Bode phase angle plots examined in several supercapacitor cells based on the 2D titanium carbo-oxide electrode in the three electrolytes. As depicted in that figure, the Bode phase angle only reached about  $-10^\circ$  at the lowest frequency, which showed the ionic resistance contributions dominated in the supercapacitor. The observed small Bode phase value is an indication of a poor insulator, which means there would be current leakage with electron flow through the dielectric separator. This also means that the material would be less able to effectively hold electric charge.<sup>57</sup> This phenomenon could be enhanced particularly with the high conductivity of this 2D titanium carbo-oxide due to the point defects created during the etching process, as already reported by H. O. Badr *et al.*<sup>28</sup> However, the phase angle increased over the high-frequency range, where a decline in phase angle response indicates an increase in ionic resistance. It is important to note that the layered structures of the 2D titanium carbo-oxide promoted the diffusion and adsorption of electrolyte ions, resulting in an attractive supercapacitor performance. Table 2 compares the supercapacitor performance of this new 2D titanium carbo-oxide material with other published works in various electrolytes. In Na<sub>2</sub>SO<sub>4</sub> for example, the energy and power densities of this material were superior to some of the reported works in the literature. The specific capacitance obtained in H<sub>2</sub>SO<sub>4</sub> for this material was also higher than some reported in the literature also. Therefore, it could be concluded that the pure 2D titanium carbo-oxide nanomaterials prepared by an eco-friendly and low-cost method in this work show superior supercapacitor characteristics.

## 4. Conclusion

In this work, we demonstrated a simple and cost-effective solvothermal method for preparing a newly developed 2D titanium carbo-oxide layered structure material. Full characterization of the as-prepared material was performed and the gas-sensing properties using electrochemical impedance spectroscopy and by assessing the supercapacitor performances were investigated. The sensor response obtained towards 1500 ppm of methanol at room temperature was 71%. The responses towards other interfering gases, such as acetone ( $\sim 18\%$ ), ethanol ( $\sim 8\%$ ), isopropanol ( $<1\%$ ), *n*-butanol ( $<1\%$ ), and toluene ( $<1\%$ ), were very low, indicating the good selectivity towards methanol. The small size of the interlayer spacing was probably the main reason for the good sensing performance. Three aqueous electrolytes were used to investigate the supercapacitor performances. The results indicated that the active electrode material had a specific capacitance of 90 F g<sup>-1</sup> (for KOH), 161 F g<sup>-1</sup> (for H<sub>2</sub>SO<sub>4</sub>), and 129 F g<sup>-1</sup> (for Na<sub>2</sub>SO<sub>4</sub>) at an applied current rate of 0.001 A. The obtained potential window was 1.25 V (with KOH), 0.85 V (with H<sub>2</sub>SO<sub>4</sub>), and 1.8 V (with Na<sub>2</sub>SO<sub>4</sub>). The best cycling stability was acquired with KOH, where the retention capacitance was 87.1% after 2500 cycles. The ion sizes, the presence of point defects, and the interlayer spacing can explain the difference recorded in the supercapacitor performances in the three chosen electrolytes. As this first work is a kind of proof of concept, some investigations are still needed (*e.g.* to assess the sensor long-term stability, effect of humidity, supercapacitor stability over 10 000 cycles) to understand and improve the material characteristics of this new 2D nanomaterial produced *via* an eco-friendly and inexpensive method. However, this material shows great promise to be applied in some other high-tech applications.

## Author contributions

Roussin Lontio Fomekong: conceptualization, data curation, methodology and investigation concerning sensor and supercapacitor testing, writing original draft; Jalal Azadmanjiri: visualization, formal analysis concerning supercapacitor, writing – review; Joyce Boitumelo Matsoso: visualization, formal analysis concerning gas sensor; Marco Serra: formal analysis



concerning SEM data curation; Sana Akir: writing – review, data curation; Lukáš Dekanovský: formal analysis concerning SEM and data curation; Jan Luxa: formal analysis concerning XPS, data curation; Eva Vejmelková: formal analysis concerning TEM, data curation. Zdeněk Sofer: conceptualization, supervision, project administration, funding acquisition, validation, writing – review and editing.

## Conflicts of interest

There are no conflicts to declare.

## Acknowledgements

R. L. F. was supported by the European Structural and Investment Funds, OP RDE-funded project 'CHEMFELLS IV' (No. CZ.02.2.69/0.0/0.0/20\_079/0017899). This work was supported by Czech Science Foundation (GACR No. 23-05918S).

## References

- I. F. U. Muzayanah, H. H. Lean, D. Hartono, K. D. Indraswari and R. Partama, *Heliyon*, 2022, **8**, e10634.
- M. M. Rahman and X.-B. Vu, *Sustainability*, 2021, **13**, 3749.
- H. Weber and J. D. Sciubba, *Eur. J. Popul.*, 2019, **35**, 379–402.
- S. H. Preston, *Popul. Res. Policy Rev.*, 1996, **15**, 95–108.
- J. P. Holdren, *Popul. Environ.*, 1991, **12**, 231–255.
- J. Mitali, S. Dhinakaran and A. A. Mohamad, *Energy Storage Sav.*, 2022, **1**, 166–216.
- A. G. Olabi, C. Onumaegbu, T. Wilberforce, M. Ramadan, M. A. Abdelkareem and A. H. Al-Alami, *Energy*, 2021, **214**, 118987.
- M. Pershaanaa, S. Bashir, S. Ramesh and K. Ramesh, *J. Energy Storage*, 2022, **50**, 104599.
- M. Şahin, F. Blaabjerg and A. Sangwongwanich, *Energies*, 2022, **15**, 674.
- G. Shaddick, M. L. Thomas, P. Mudu, G. Ruggeri and S. Gumy, *npj Clim. Atmos. Sci.*, 2020, **3**, 23.
- J. Gonzalez-Martin, N. J. R. Kraakman, C. Perez, R. Lebrero and R. Munoz, *Chemosphere*, 2021, **262**, 128376.
- E. David and V. C. Niculescu, *Int. J. Environ. Res. Public Health*, 2021, **18**, 13147.
- Z. Nekoukar, Z. Zakariaei, F. Taghizadeh, F. Musavi, E. S. Banimostafavi, A. Sharifpour, N. Ebrahim Ghuchi, M. Fakhar, R. Tabaripour and S. Safanavaei, *Ann. Med. Surg.*, 2021, **66**, 102445.
- B. Saruhan, R. Lontio Fomekong and S. Nahirniak, *Front. Sens.*, 2021, **2**, 657931.
- H. Yu, C. Guo, X. Zhang, Y. Xu, X. Cheng, S. Gao and L. Huo, *Adv. Sustainable Syst.*, 2022, **6**, 2100370.
- K. K. Patel, T. Singhal, V. Pandey, T. P. Sumangala and M. S. Sreekanth, *J. Energy Storage*, 2021, **44**, 103366.
- L.-Å. Näslund, P. O. Å. Persson and J. Rosen, *J. Phys. Chem. C*, 2020, **124**, 27732–27742.
- D. Lahem, F. R. Lontio, A. Delcorte, L. Bilteryst and M. Debliquy, *IOP Conf. Ser.: Mater. Sci. Eng.*, 2016, **108**, 012002.
- S. M. Oh and S.-J. Hwang, *J. Korean Ceram. Soc.*, 2020, **57**, 119–134.
- J. Zhang, L. Liu, Y. Yang, Q. Huang, D. Li and D. Zeng, *Phys. Chem. Chem. Phys.*, 2021, **23**, 15420–15439.
- G. Murali, J. Rawal, J. K. R. Modigunta, Y. H. Park, J.-H. Lee, S.-Y. Lee, S.-J. Park and I. In, *Sustainable Energy Fuels*, 2021, **5**, 5672–5693.
- S. Nahirniak and B. Saruhan, *Sensors*, 2022, **22**, 972.
- R. Ma, Z. Chen, D. Zhao, X. Zhang, J. Zhuo, Y. Yin, X. Wang, G. Yang and F. Yi, *J. Mater. Chem. A*, 2021, **9**, 11501–11529.
- J. Li, X. Yuan, C. Lin, Y. Yang, L. Xu, X. Du, J. Xie, J. Lin and J. Sun, *Adv. Energy Mater.*, 2017, **7**, 1602725.
- A. Khosla Sonu, H. T. A. Awan, K. Singh Gaurav, R. Walvekar, Z. Zhao, A. Kaushik, M. Khalid and V. Chaudhary, *Adv. Sci.*, 2022, **9**, e2203527.
- A. Palacios-Adrós, M. Altomare, A. Tighineanu, R. Kirchgorg, N. K. Shrestha, I. Diez-Pérez, F. Caballero-Briones, F. Sanz and P. Schmuki, *J. Mater. Chem. A*, 2014, **2**, 915–920.
- X. Li, Z. An, Y. Lu, J. Shan, H. Xing, G. Liu, Z. Shi, Y. He, Q. Chen, R. P. S. Han, D. Wang, J. Jiang, F. Zhang and Q. Liu, *Adv. Mater. Technol.*, 2021, **7**, 2100872.
- H. O. Badr, T. El-Melegy, M. Carey, V. Natu, M. Q. Hassig, C. Johnson, Q. Qian, C. Y. Li, K. Kushnir, E. Colin-Ulloa, L. V. Titova, J. L. Martin, R. L. Grimm, R. Pai, V. Kalra, A. Karmakar, A. Ruffino, S. Masiuk, K. Liang, M. Naguib, O. Wilson, A. Magenau, K. Montazeri, Y. Zhu, H. Cheng, T. Torita, M. Koyanagi, A. Yanagimachi, T. Ouisse, M. Barbier, F. Wilhelm, A. Rogalev, J. Björk, P. O. Å. Persson, J. Rosen, Y.-J. Hu and M. W. Barsoum, *Mater. Today*, 2022, **54**, 8–17.
- Y. Jiang, L. Cao, X. Hu, Z. Ren, C. Zhang and C. Wang, *Inorg. Chem.*, 2018, **57**, 15123–15132.
- Y. Qin, J. Wang and Y. Bai, *Phys. Status Solidi A*, 2021, **218**, 2000642.
- L. Malepe, D. T. Ndinteh, P. Ndungu and M. A. Mamo, *RSC Adv.*, 2022, **12**, 27094–27108.
- S. Singh and S. Sharma, *Sens. Actuators, B*, 2022, **350**, 130798.
- S. Das, S. Sharma and S. K. Sharma, *IEEE Sens. J.*, 2019, **19**, 9090–9096.
- C. Wang, X. Kou, N. Xie, L. Guo, Y. Sun, X. Chuai, J. Ma, P. Sun, Y. Wang and G. Lu, *ACS Sens.*, 2017, **2**, 648–654.
- L. Li, J. Li, W. Fu, D. Jiang, Y. Song, Q. Yang, W. Zhu and J. Zhang, *Nanotechnology*, 2022, **33**, 252001.
- J. B. Matsoso, N. Antonatos, P. R. Kumar, C. Jellett, V. Mazánek, C. Journet and Z. Sofer, *J. Mater. Chem. C*, 2022, **10**, 3307–3317.
- P. J. Maake, T. P. Mokoena, A. S. Bolokang, N. Hintsho-Mbita, J. Tshilongo, F. R. Cummings, H. C. Swart, E. I. Iwuoha and D. E. Motaung, *Mater. Adv.*, 2022, **3**, 7302–7318.
- K. Yang, K. Cho, D. S. Yoon and S. Kim, *Sci. Rep.*, 2017, **7**, 40163.
- B. Pal, S. Yang, S. Ramesh, V. Thangadurai and R. Jose, *Nanoscale Adv.*, 2019, **1**, 3807–3835.



- 40 Z. Pan, F. Cao, X. Hu and X. Ji, *J. Mater. Chem. A*, 2019, **7**, 8984–8992.
- 41 Q. Wang, S. Wang, X. Guo, L. Ruan, N. Wei, Y. Ma, J. Li, M. Wang, W. Li and W. Zeng, *Adv. Electron. Mater.*, 2019, **5**, 1900537.
- 42 W. Liu, Z. Wang, Y. Su, Q. Li, Z. Zhao and F. Geng, *Adv. Energy Mater.*, 2017, **7**, 1602834.
- 43 Y. Wang, X. Wang, X. Li, R. Liu, Y. Bai, H. Xiao, Y. Liu and G. Yuan, *Nanomicro Lett.*, 2020, **12**, 115.
- 44 J. Yan, C. E. Ren, K. Maleski, C. B. Hatter, B. Anasori, P. Urbankowski, A. Sarycheva and Y. Gogotsi, *Adv. Funct. Mater.*, 2017, **27**, 1701264.
- 45 Z. Fan, Y. Wang, Z. Xie, D. Wang, Y. Yuan, H. Kang, B. Su, Z. Cheng and Y. Liu, *Adv. Sci.*, 2018, **5**, 1800750.
- 46 Z. Pan and X. Ji, *J. Power Sources*, 2019, **439**, 227068.
- 47 J. Fu, J. Yun, S. Wu, L. Li, L. Yu and K. H. Kim, *ACS Appl. Mater. Interfaces*, 2018, **10**, 34212–34221.
- 48 A. M. Navarro-Suárez, K. L. Van Aken, T. Mathis, T. Makaryan, J. Yan, J. Carretero-González, T. Rojo and Y. Gogotsi, *Electrochim. Acta*, 2018, **259**, 752–761.
- 49 D. Jiménez-Cordero, F. Heras, M. A. Gilarranz and E. Raymundo-Piñero, *Carbon*, 2014, **71**, 127–138.
- 50 H. He, J. Wang, Q. Xia, L. Wang, Q. Hu and A. Zhou, *Appl. Surf. Sci.*, 2021, **568**, 150971.
- 51 S. Venkateshalu, J. Cherusseri, M. Karnan, K. S. Kumar, P. Kollu, M. Sathish, J. Thomas, S. K. Jeong and A. N. Grace, *ACS Omega*, 2020, **5**, 17983–17992.
- 52 Y. Tang, J. Zhu, C. Yang and F. Wang, *J. Electrochem. Soc.*, 2016, **163**, A1975–A1982.
- 53 P. Staiti, A. Arenillas, F. Lufrano and J. Á. Menéndez, *J. Power Sources*, 2012, **214**, 137–141.
- 54 S. A. Patil, I. Rabani, S. Hussain, Y. S. Seo, J. Jung, N. K. Shrestha, H. Im and H. Kim, *Nanomaterials*, 2022, **12**, 339.
- 55 J. Azadmanjiri, L. Děkanovský, S. Wei, M. Li and Z. Sofer, *J. Energy Storage*, 2022, **56**, 105918.
- 56 M. Pathak, S. R. Polaki and C. S. Rout, *RSC Adv.*, 2022, **12**, 10788–10799.
- 57 N. O. Laschuk, E. B. Easton and O. V. Zenkina, *RSC Adv.*, 2021, **11**, 27925–27936.

